



# Towards the connection between snow microphysics and melting layer: Insights from multi-frequency and dual-polarization radar observations during BAECC

Haoran Li<sup>1</sup>, Jussi Tiira<sup>1</sup>, Annakaisa von Lerber<sup>2</sup>, and Dmitri Moisseev<sup>1,2</sup>

<sup>1</sup>Institute for Atmospheric and Earth System Research / Physics, Faculty of Science, University of Helsinki, Finland

<sup>2</sup>Finnish Meteorological Institute, Helsinki, Finland

**Correspondence:** Haoran Li (haoran.li@helsinki.fi)

**Abstract.** In stratiform rainfall, the melting layer is often visible in radar observations as an enhanced reflectivity band, the so-called bright band. Despite the ongoing debate on the exact microphysical processes taking place in the melting layer and on how they translate into radar measurements, both model simulations and observations indicate that the radar-measured melting layer properties are influenced by snow microphysical processes that take place above it. There is still, however, a lack of comprehensive observations to link the two. To advance our knowledge of precipitation formation in ice clouds and provide an additional constraint on the retrieval of ice cloud microphysical properties, we have investigated this link. This study is divided into two parts. Firstly, surface-based snowfall measurements are used to devise a method for classifying rimed and unrimed snow from X- and Ka-band Doppler radar observations. In the second part, this classification is used in combination with multi-frequency and dual-polarization radar observations to investigate the impact of precipitation intensity, aggregation, riming, and dendritic growth on melting layer properties. The radar-observed melting layer characteristics show strong dependence on precipitation intensity as well as detectable differences between unrimed and rimed snow. This study is based on data collected during the Biogenic Aerosols - Effects on Clouds and Climate (BAECC) experiment, which took place in 2014 in Hyytiälä, Finland.

## 1 Introduction

Stratiform precipitation is prevalent in mid- to high- latitudes. In such precipitation systems, ice particles nucleated at the cloud top descend and grow on their way down by going through various microphysical processes, e.g., vapor deposition, aggregation and/or riming (Lamb and Verlinde, 2011). In the case of rainfall, these ice particles transform into raindrops in the melting layer (ML). The melting of ice particles is capable of modulating the thermal structure of the ML through the exchange of latent heat with the environment (Stewart et al., 1984; Carlin and Ryzhkov, 2019) and, as a result, can change the dynamics of precipitation (e.g., Heymsfield, 1979; Szeto et al., 1988; Fabry and Zawadzki, 1995). It has been shown that ML properties are modified by the ambient environment (Carlin and Ryzhkov, 2019) as well as microphysical processes taking place in the ML (Heymsfield et al., 2015), and by snow microphysical processes occurring above, e.g., aggregation and riming (Stewart et al., 1984; Klaassen, 1988; Fabry and Zawadzki, 1995; Zawadzki et al., 2005; von Lerber et al., 2014; Kumjian et al., 2016;



Xie et al., 2016; Wolfensberger et al., 2016; Trömel et al., 2019). In addition, the microwave attenuation in the ML is sensitive to the parameterization of snow microphysics (von Lerber et al., 2014) and can be significant at mm-wavelength (Matrosov, 2008; Haynes et al., 2009; Li and Moisseev, 2019).

To cm-wavelength weather radars, the ML appears as a band of the increased reflectivity, the so-called bright band, while to mm-wavelength radars such appearance is less distinct (e.g., Lhermitte, 1988; Sassen et al., 2005; Kollias and Albrecht, 2005). Properties of the ML and its radar manifestation bright band are influenced by cloud dynamics and microphysics, which can be directly probed by aircraft-mounted in-situ measurements (e.g., Stewart et al., 1984; Willis and Heymsfield, 1989; Heymsfield et al., 2015) despite the inability to conduct continuous long-term operation with such setups. Remote sensing of the ML with radars dates back to the 1940s (Ryde, 1946). Atlas (1957) have found that the strength of the bright band is weakened when melting graupel particles present, which was further confirmed by Klaassen (1988) and Zawadzki et al. (2005). A comprehensive long-term analysis of the ML appearance in vertically pointing X-band radar and UHF wind profiler observations has been performed by Fabry and Zawadzki (1995). They have compiled a record of the main ML features that were later used in modeling studies (e.g., Szyrmer and Zawadzki, 1999; Zawadzki et al., 2005; von Lerber et al., 2014). As the ML bridges snow and rain, the raindrop size distributions below the ML seem to be related to the bright band's reflectivity values (Huggel et al., 1996; Sarma et al., 2016). As presented by Wolfensberger et al. (2016), the thickness of the ML depends on riming, particle fall velocities as well as the bright band intensity. Meanwhile, the downward extension of the bright band, called the saggy bright band, may be linked to riming as suggested by previous studies (Trömel et al., 2014; Kumjian et al., 2016; Ryzhkov et al., 2016; Xie et al., 2016; Erlingis et al., 2018). Recently, Carlin and Ryzhkov (2019) have incorporated the cooling effects of melting snowflakes in the ML model and proposed that the saggy bright band may be explained by a combination of processes instead of a single factor. From the perspective of observation, there seems to be a lack of statistical studies untangling the impacts of snow growth processes on the observed ML properties.

Over the last few years, multi-frequency radar measurements of clouds and precipitation have become more easily attainable, which has led to the proliferation of studies demonstrating the advantages of using these observations for the investigation of snow microphysical processes (e.g., Kneifel et al., 2011, 2015; Leinonen et al., 2012a, 2013, 2018; Tyynelä and Chandrasekar, 2014; Leinonen and Moisseev, 2015; Leinonen and Szyrmer, 2015; Grecu et al., 2018; Chase et al., 2018; Mason et al., 2018, 2019). The potential dependence of dual-wavelength ratios (DWRs) at Ka-W-bands and X-Ka-bands on riming was observed by Kneifel et al. (2015). Dias Neto et al. (2019) have presented the strong aggregation signatures close to the ML using multi-frequency radar observations. This rapid aggregation could manifest itself as a dark band in W-band cloud radar observations, namely the dip of radar reflectivity just above the ML top (Lhermitte, 1988; Sassen et al., 2005, 2007; Heymsfield et al., 2008). Such reflectivity dip just above the ML may even be present in X-band radar measurements of light precipitation (Fabry and Zawadzki, 1995) but has not been well addressed. Mason et al. (2018) have incorporated the Doppler velocity and radar reflectivity observations from vertically-pointing Ka- and W-band radars into an optimal estimation scheme to infer the riming fraction, among other parameters. In addition to multi-frequency radar observations, dual-polarization radar measurements show promise in improving our understanding of ice precipitation processes (e.g., Bechini et al., 2013; Giangrande et al., 2016; Kumjian et al., 2016; Ryzhkov et al., 2016; Moisseev et al., 2015, 2017; Li et al., 2018; Oue et al., 2018; Vogel and Fabry, 2018;



Moisseev et al., 2019; Tiira and Moisseev, 2020). Therefore, the utilization of collocated multi-frequency and dual-polarization radar observations may pave the way for a better understanding of the connection between dry and melting snow microphysics.

During the Biogenic Aerosols Effects on Clouds and Climate (BAECC) experiment (Petäjä et al., 2016), vertically-pointing X-, Ka- and W-band cloud radars were deployed at the University of Helsinki research station in Hyttiälä, Finland. These observations were supplemented by Range-Height Indicator (RHI) scans carried out by the Finnish Meteorological Institute (FMI) C-band dual-polarization radar, providing a set of unique synergistic observations ideally suited to studying the connection between the growth and melting processes of snowflakes.

The paper is organized as follows. Section 2 introduces the instrumentation used in this study, followed by the illustration of detecting the ML and separating unrimed and rimed snow in Sect. 3. A sanity check of the snow classification and the statistical results of multi-frequency and dual-polarization radar observations are provided in Sect. 4. Conclusions are presented in Sect. 5.

## 2 Measurements

The BAECC field campaign was conducted at the University of Helsinki Hyttiälä Station from February to September 2014 (Petäjä et al., 2016). This experiment provides comprehensive vertically-pointing multi-frequency radar rainfall observations, which are used in this study. A 2D-video disdrometer (2DVD) was used to measure rain rate and calibrate X-band radar reflectivity. The collocated observations were aided by the FMI C-band dual-polarization weather radar. In addition to the radar setup during BAECC, long-term snow observations were made by a National Aeronautics and Space Administration (NASA) Particle Imaging Package (PIP, Newman et al., 2009; Tiira et al., 2016; von Lerber et al., 2017).

### 2.1 2DVD and vertically-pointing radars

The ARM 2DVD used in this study is a new generation of the one described in (Kruger and Krajewski, 2002). It relies on two cameras as well as two light sources placed in orthogonal directions and records image projections of raindrops as they fall cross the cameras' field of view. The 2DVD is often used for recording the size distributions, fall velocities and shapes of raindrops. Based on these information, the rain rate and reflectivity at a given radar frequency can be derived.

The X/Ka-band scanning Atmospheric Radiation Measurement (ARM) cloud radar (X/Ka-SACR) and W-band ARM cloud radar (MWACR) have the range gate spacing of 25 m, 25 m and 30 m, respectively (Kollias et al., 2014; Kneifel et al., 2015; Falconi et al., 2018). The original time resolution of 2 s was averaged to 10 s for these radars. The half-power beam widths of X-SACR, Ka-SACR and MWACR are 1.27°, 0.33° and 0.38°, respectively. X- and Ka-SACR are dual-polarization radar systems installed on the same pedestal, recording the co-polar (e.g.,  $\rho_{hv}$ ,  $Z_{dr}$ ) and cross-polar (e.g., cross-polar correlation coefficient, linear depolarization ratio LDR) measurements, respectively. MWACR had a small antenna pointing error of 0.5° to 1°, which may lead to significant error in the vertical Doppler velocity which, but does not affect reflectivity measurements.

To mitigate the potential attenuation from wet radome and raindrops, the simulated X-band radar reflectivity from 2DVD data was used to match the measured X-band reflectivity at 500 m where the near-field effect is minimized (Sekelsky, 2002;



Falconi et al., 2018). During BA ECC, a radiosonde was launched four times per day, out of which the temporally closest one was used as input to the millimeter-wave propagation model (Liebe, 1985) to correct for the gaseous attenuation at all radar frequencies.

## 2.2 Dual-polarization weather radar

5 The FMI C-band dual-polarization weather radar located in Ikaalinen, 64 km west from the Hyttiälä station, operates in the simultaneous transmission and receiving mode (Doviak et al., 2000). This radar performs RHI scans over the measurement site every 15 minutes. The range and azimuth resolutions are 500 m and  $1^\circ$ , respectively. The dual-polarization measurements used in this study are  $Z_{dr}$ , which was calibrated during light rainfalls (Bringi and Chandrasekar, 2001; Li et al., 2018). For data analysis, the Python ARM Radar Toolkit (Helmus and Collis, 2016) was used.

## 10 2.3 NASA Particle Imaging Package

The PIP is an improved version of the Snowflake Video Imager (Newman et al., 2009), which uses a high frame rate camera, operating at 380 frames per second, to record the silhouettes of precipitation particles. The field of view of this camera is  $48 \times 64$  mm with a spatial resolution of  $0.01 \text{ mm}^2$ . The focal plane of this camera is 1.3 m. Because the measurement volume is not enclosed, the wind-induced effects on the measurements are minimized (Newman et al., 2009). The data-processing software  
15 defines the size of each particle using the disk-equivalent diameter ( $D_{deq}$ ) which is the diameter of a disk with the same area of a particle shadow. Particle size distribution (PSD) and fall velocity are recorded as a function of  $D_{deq}$  in the PIP software. Based on these PIP products, von Lerber et al. (2017) have derived particle mass and fall velocity as a function of the observed maximum particle diameter ( $D_{max, ob}$ ), which is obtained by fitting an ellipsoid model to each particle. Here and hereafter,  $D$  represents  $D_{max, ob}$ . In this study, snow observations for the winter of 2014-2018 were processed using the method by von  
20 Lerber et al. (2017).

## 3 Methods

### 3.1 Detection of ML boundaries

The height where melting starts ranges from the surface to several km above, mainly depending on the temperature profiles. Thus, prior to addressing the general characteristics of ML, it is important to detect ML boundaries. Fabry and Zawadzki  
25 (1995) have employed the gradient of reflectivity to determine the ML boundaries using single-polarization X-band radar measurements. The vertically-pointing X-/Ka-band radars used in this study provide dual-polarization observations, i.e.  $\rho_{hv}$  and LDR, respectively. These observations supply additional information to estimate the ML boundaries (Giangrande et al., 2008). However, care should be taken in how this information is used. Wolfensberger et al. (2016) have suggested the use of  $\rho_{hv}$  could underestimate the ML top, as the significant drop in  $\rho_{hv}$  may not happen until a significant amount of ice has  
30 already melted. To mitigate this issue, we determined the upper boundary of ML by finding the local minimum of the X-band



reflectivity gradient around the  $\rho_{\text{hv}}$ -detected ML top, which is similar to (Wolfensberger et al., 2016). The ML bottom was determined in a similar way to derive the radar reflectivity at the melting bottom. Note that cases where precipitation fall streaks are significantly slanted, as shown in (Fabry and Zawadzki, 1995), were excluded.

### 3.2 Diagnosing snowflake rime mass fraction

- 5 The rime mass fraction (FR), defined as the ratio of accreted ice mass by riming to the total snowflake mass, has been used to quantify the riming extent in ice microphysical schemes (Morrison and Milbrandt, 2015) and in observational studies (e.g., Moisseev et al., 2017; Li et al., 2018). The rime mass fraction can be defined as

$$\text{FR} = 1 - \frac{\int_{D_{\min}}^{D_{\max}} N(D)m_{\text{ur}}(D)dD}{\int_{D_{\min}}^{D_{\max}} N(D)m_{\text{ob}}(D)dD} \quad (1)$$

- where  $D_{\max}$  and  $D_{\min}$  are maximum and minimum particle sizes, respectively,  $m_{\text{ob}}(D)$  and  $m_{\text{ur}}(D)$  are masses of observed and unrimed snowflakes as a function of  $D$ , respectively, and  $N(D)$  is the PSD. In this study, FR was computed using ground-based observations of PSD and snowflake masses retrieved from PIP observations as described in (von Lerber et al., 2017). The masses of unrimed ice particles were derived assuming the following. Firstly, unrimed snowflakes were present in PIP observations. Secondly, the ice particles belonging to the lightest 5% are representative of unrimed snowflakes. Following these assumptions, the mass-dimension relation  $m_{\text{us}}(D) = 0.0053D^{2.05}$  that is representative of unrimed snowflakes was derived. Further discussion on the definition of  $m_{\text{us}}(D)$  is referred to (Moisseev et al., 2017) and (Li et al., 2018).

Mason et al. (2018) have shown that the extent of riming can be retrieved using radar-measured DWR (Matrosov, 1998; Hogan et al., 2000) and mean Doppler velocity ( $V$ ). If the radar reflectivity is expressed in dB, then the DWR can be written as

$$\text{DWR}(\lambda_1, \lambda_2) = Z_{\lambda_1} - Z_{\lambda_2} \quad (2)$$

where  $Z_{\lambda_1}$  and  $Z_{\lambda_2}$  are observed radar reflectivities at the wavelength of  $\lambda_1$  and  $\lambda_2$ , respectively.  $Z_{\lambda}$  can be expressed as

$$Z_{\lambda} = 10 \log_{10} \left( \int_{D_{\min}}^{D_{\max}} \frac{\lambda^4}{\pi^5 |K_{\lambda}|^2} N(D) \sigma_{b,\lambda}(D, m_{\text{ob}}(D)) dD \right) \quad (3)$$

where  $|K_{\lambda}|^2$  is the dielectric constant of liquid water, and  $\sigma_{b,\lambda}(D, m_{\text{ob}}(D))$  is the backscattering coefficient of snow particles at a given wavelength. In X-SACR, Ka-SACR and MWACR data files  $|K_{\lambda}|^2$  is set to 0.93, 0.88, and 0.70, respectively. The values of  $\sigma_{b,\lambda}$  were taken from the single-scattering databases (Leinonen and Moisseev, 2015; Leinonen and Szyrmer, 2015; Tyynelä and von Lerber, 2019). These three datasets were combined into a single lookup table of ice particle scattering properties



defined as a function of maximum diameter and mass. For given  $D$  and  $m_{\text{ob}}$ , the backscattering cross section was estimated using linear interpolation in the log-log space. The mean Doppler velocity can be derived in the same way,

$$V_{\lambda} = \frac{\int_{D_{\min}}^{D_{\max}} v(D)N(D)\sigma_{b,\lambda}(D, m_{\text{ob}}(D))dD}{\int_{D_{\min}}^{D_{\max}} N(D)\sigma_{b,\lambda}(D, m_{\text{ob}}(D))dD} \quad (4)$$

where  $v(D)$  is the fall velocity of snowflakes with the same  $D$  and can be derived together with  $m(D)$  following (von Lerber et al., 2017). To minimize the impact of varying air density ( $\rho_{\text{air}}$ ),  $V_{\lambda}$  was adjusted to the air condition of 1000 hPa and 0°C (air density  $\rho_{\text{air},0}$ ) with a factor of  $(\frac{\rho_{\text{air},0}}{\rho_{\text{air}}})^{0.54}$  (Heymsfield et al., 2007).  $\rho_{\text{air}}$  was derived from the temperature and relative humidity obtained from the temporally closest sounding.

Dias Neto et al. (2019) have shown that the size growth of snowflakes close to the ML is accelerated due to the enhanced aggregation. Therefore, relatively large aggregates are prevalent snow types close to the ML, and are better represented by DWR(X,Ka) than DWR(Ka,W) (see the comparison by Barrett et al., 2019). The use of lower radar frequency (X- and Ka-bands) avoids estimating the non-neglectable W-band attenuation caused by ML as well as supercooled liquid water (Li and Moisseev, 2019). Therefore, the potential link between FR and simulated Doppler radar measurements at X- and Ka bands was accessed, with the utilization of in-situ snowfall observations from BAEC to the winters of 2014-2018.

The dependence of DWR(X, Ka) and  $V_X$  on FR can be computed using Eq. (1), (2) and (4). For comparison, the  $m_{\text{ob}} - D$  and  $v - D$  relations of aggregates of unrimed radiating assemblages, side planes, bullets and columns (LH74 unrimed), aggregates of densely rimed radiating assemblages of dendrites (LH74 rimed) and lump graupel (LH74 graupel) presented in (Locatelli and Hobbs, 1974) were used. To compute the DWR(X, Ka) and  $V_X$  using the literature relations, we assumed that  $N(D)$  can be parameterized as

$$N(D) = N_0 e^{-\Lambda D} \quad (5)$$

here the intercept parameter  $N_0$  cancels out while computing DWR and  $V_X$ , so the radar variables depend on  $\Lambda$ , which controls the average size of ice particles in  $N(D)$ . We have varied  $\Lambda^{-1}$  between 0 and 11 mm to mimic different snowfall conditions, which is similar to what was done in (Leinonen and Szyrmer, 2015). Table 1 summaries the fitted expressions of  $\text{DWR}(X, Ka) = aV_X^b$  for these three particle types. Since snow microphysics as well as the corresponding radar measurements can significantly change with precipitation intensity (Moisseev et al., 2017), the computed values were separated into four subgroups according to precipitation rate (PR).

Simulations of  $\text{DWR}(X,Ka)-V_X$  for four groups of precipitation rate are presented in Fig. 1. Most cases with  $\text{FR} \leq 0.2$  are centered around the curve of LH74 unrimed, whose velocity-diameter relation is similar with low density snowflakes (Tiira et al., 2016). It seems that riming happens more frequently in heavier precipitation. In contrast, much fewer unrimed cases are present in heavier precipitation (Fig. 1 c,d). Heavily rimed snowflakes ( $\text{FR} > 0.5$ , red dots) are characterized by low  $\text{DWR}(X,Ka)$  and high  $V_X$ , contrasting with the unrimed/lightly rimed cases (blue dots). Specifically, snowflakes with large sizes and low velocities usually are rather slightly rimed ( $\text{FR} \leq 0.2$ ). For the cases where FR exceeds 0.5, most  $\text{DWR}(X,Ka)$

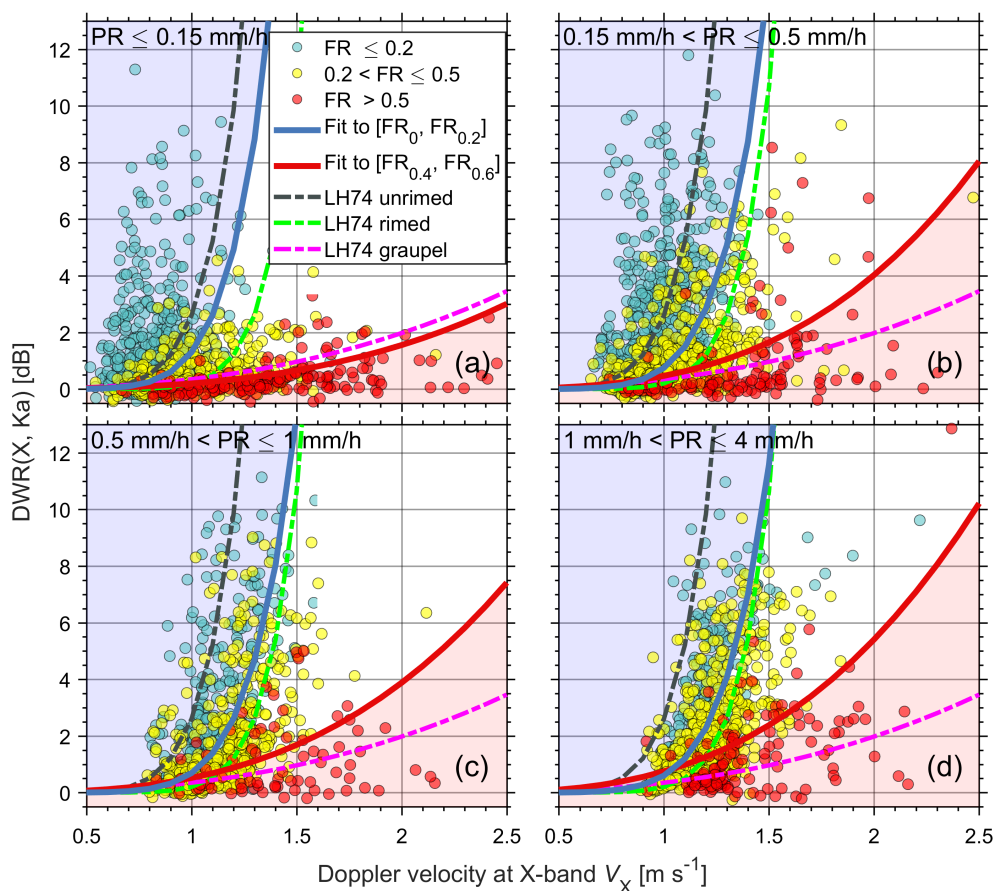


**Figure 1.** Scatter plot of DWR(X,Ka) vs.  $V_X$  (1000 hPa and  $0^\circ\text{C}$ ) colored with FR. Mass-size and velocity-size relations from (Locatelli and Hobbs, 1974) are adopted for reference (dashed lines). Observed mass-size and velocity-size relations are derived using the approach developed by von Lerber et al. (2017), and the particle back-scattering coefficient  $\sigma_{b,\lambda}$  is adopted from (Leinonen and Moisseev, 2015; Leinonen and Szyrmer, 2015). The solid blue and red curves separate unrimed (light blue shading), transitional (no shading) and rimed snow (light red shading) in our classification scheme.

values are below 3 dB, indicating that heavily rimed particles are usually associated with small snowflakes. Inspired by this distinct feature, we have fitted the  $DWR(X, Ka) = aV_X^b$  relations for cases with  $FR \leq 0.2$  and  $0.4 \leq FR \leq 0.6$  (shown in Table 1), which separate the observations into three types: unrimed, transitional and rimed snow. For the sake of comparison, the power  $b$  for unrimed snow was adopted from the fit for LH74 unrimed. In this study, these fitted relations were employed for classifying unrimed and rimed snow. Also, since the derived DWR(X,Ka) can be affected by supercooled liquid water among other factors, cases with  $DWR(X,Ka) < 1$  dB were rejected when identifying unrimed snow.



**Table 1.** Fitted parameters for  $DWR(X, Ka) = aV_X^b$

Fitted parameters		$a$	$b$
LH74	unrimed	2.6	7.3
	rimed	0.2	9.8
	graupel	0.35	2.5
$PR \leq 0.15 \text{ mm h}^{-1}$	$FR \in [0 \ 0.2]$	1.3	7.3
	$FR \in [0.4 \ 0.6]$	0.2	2.96
$0.15 \text{ mm h}^{-1} < PR \leq 0.5 \text{ mm h}^{-1}$	$FR \in [0 \ 0.2]$	0.75	7.3
	$FR \in [0.4 \ 0.6]$	0.47	3.1
$0.5 \text{ mm h}^{-1} < PR \leq 1 \text{ mm h}^{-1}$	$FR \in [0 \ 0.2]$	0.69	7.3
	$FR \in [0.4 \ 0.6]$	0.52	2.9
$1 \text{ mm h}^{-1} < PR \leq 4 \text{ mm h}^{-1}$	$FR \in [0 \ 0.2]$	0.6	7.3
	$FR \in [0.4 \ 0.6]$	0.75	2.85

## 4 Results

To study how ML properties depend on the precipitation intensity, snowflake riming fraction and PSD, all rainfall cases observed during the BAECC experiment were analyzed. Given the need for coinciding multi-frequency vertically pointing radar measurements and the radar scans performed during the experiment, we have identified 4147 vertical profiles of observations in stratiform rainfall events corresponding to about 11.5 h where the measurement requirements were met. During the analysis, the mean radar Doppler velocity was scaled to the air density at 1000 hPa and 0°C as previously described. It should be noted that the RHI scans by the FMI C-band weather radar were performed every 15 min. Therefore, the profiles of specific differential phase and differential reflectivity are recorded much less frequently than the vertically-pointing radar observations. The RHI observations are nonetheless presented here in order to link the features observed in this study to the previous reports (Giangrande et al., 2016; Kumjian et al., 2016; Li et al., 2018; Vogel and Fabry, 2018).

### 4.1 Sanity check of the snow classification

At the first step of our data analysis, the classification of unrimed and rimed snow using  $DWR(X, Ka) - V_X$  observations, proposed in the previous section, was evaluated against previous studies. As shown in Fig. 2, both  $DWR(X, Ka)$  and  $V_X$  tend to increase as the precipitation intensifies. Most cases of rimed snow fall in the region where  $DWR(X, Ka) < 4 \text{ dB}$  and  $V_X$  is higher than for unrimed snow. The  $V_X$  of unrimed snow rarely exceeds 1.5 m/s. Those outliers of rimed snow in Fig. 1 (a) may be attributed to the local vertical air motions, which contaminate the measured mean Doppler velocity. It should be noted



that the snow observations in Fig. 1 are limited to  $PR \leq 4 \text{ mm h}^{-1}$ , namely the maximum radar reflectivity at the ML bottom ( $Z_{X,\text{rain}}$ ) is around 33 dBZ, as computed by using the localized  $Z - R$  relation (Leinonen et al., 2012b).

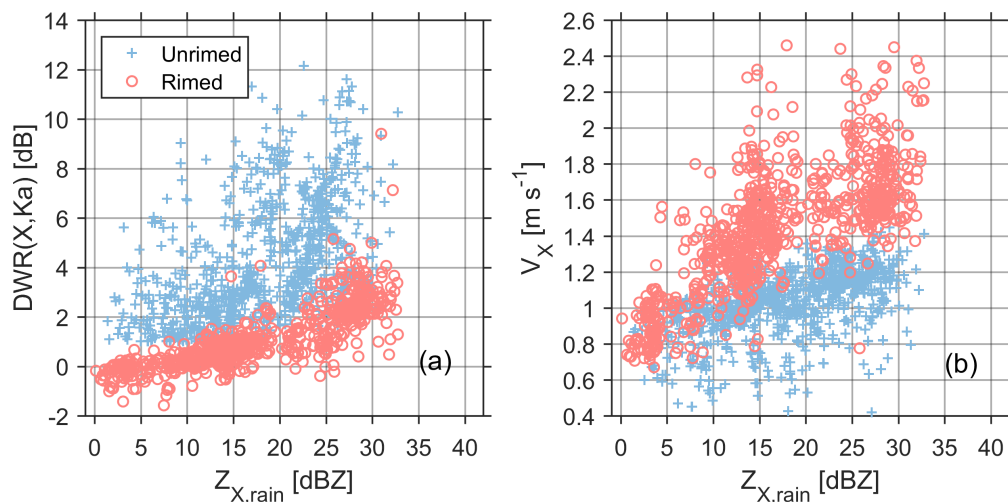


**Figure 2.** Distribution of (a)  $DWR(X, Ka)$  and (b)  $V_X$  above the ML as a function of  $Z_{X,\text{rain}}$ . Note that no transitional snow type between unrimed and rimed is presented.

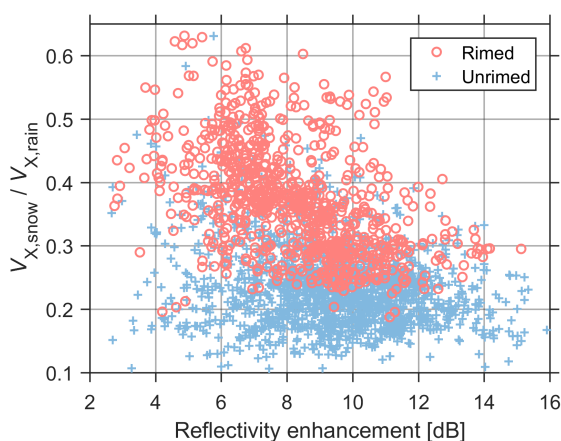


**Figure 3.** Scatter plot of  $V_{X,\text{snow}}/V_{X,\text{rain}}$  vs. reflectivity enhancement in the ML

The reflectivity enhancement in the ML, which is defined as the difference between the  $Z_X$  maximum in the ML and the  $Z_X$  at the melting bottom ( $Z_{X,\text{rain}}$ ), was also studied. Zawadzki et al. (2005) have analyzed the UHF Doppler wind profiler observations in  $V_{\text{UHF},\text{snow}}/V_{\text{UHF},\text{rain}}$ - reflectivity enhancement space and found that the augmentation of rimed snowflake mass can increase  $V_{\text{UHF},\text{snow}}/V_{\text{UHF},\text{rain}}$  and decrease reflectivity enhancement. As shown in Fig. 3, despite the scattered distribution of reflectivity enhancement, the majority of cases with high  $V_{X,\text{snow}}/V_{X,\text{rain}}$  are dominated by rimed snow while most unrimed



cases are below  $V_{X,\text{snow}}/V_{X,\text{rain}} = 0.25$ . Such dependence of  $V_{X,\text{snow}}/V_{X,\text{rain}}$  on riming is in line with the results in (Zawadzki et al., 2005), indicating the reasonable snow classification employed in this study.

## 4.2 Vertically profiles of multi-frequency radar measurements in ML

To obtain a general idea of how the ML is modulated by riming and aggregation, statistics of vertically-pointing radar observations were made. As the ML properties are modulated by precipitation intensity (Fabry and Zawadzki, 1995; Carlin and Ryzhkov, 2019), the observations were grouped by PR. In this paper, the vertical axis is shifted such that the reference height is the ML top.

### 4.2.1 X-band reflectivity, $\rho_{\text{hv}}$ and DWR(X,Ka)

Figure 4 shows the profiles of radar reflectivity and  $\rho_{\text{hv}}$  measured by X-SACR and grouped by PR. Note that to generalize the observations, the vertical axis is shifted such that the ML top is the reference height of 0 m, and each reflectivity profile was normalized by offsetting the difference between  $Z_{X,\text{rain}}$  and the median value of  $Z_{X,\text{rain}}$  in the corresponding PR group. The same procedure was made to  $\rho_{\text{hv}}$  and the following measurements. For most cases, the relative humidity (RH) around the ML top is above 95% with no dependence on PR. Thus, the effect of dry air infiltration, e.g., decreasing reflectivity and ML thickness, descending dual-polarization measurements (Carlin and Ryzhkov, 2019), should be minimized. Considering the general aspects of Fig. 4, it is clear that the ML thickness and reflectivity peak increase with PR, which is inline with previous results (Fabry and Zawadzki, 1995; Wolfensberger et al., 2016; Trömel et al., 2019).

The  $\rho_{\text{hv}}$  and radar reflectivity have been used in identifying the bright band sagging (Kumjian et al., 2016; Ryzhkov et al., 2016; Xie et al., 2016). When  $\text{PR} > 1 \text{ mm h}^{-1}$ , the level of  $\rho_{\text{hv}}$  minimum of rimed snow seems to be lower than the unrimed, however, the opposite holds when  $\text{PR} \leq 1 \text{ mm h}^{-1}$  which seems controversial to the expectation that the bright band sagging is mainly caused by riming (Kumjian et al., 2016). In our observations, both  $\rho_{\text{hv}}$  dip and reflectivity peak descend with the increase of PR. Therefore, it appears that precipitation intensity is an important factor affecting the formation of the saggy bright band. This finding is inline with a recent simulation study (Carlin and Ryzhkov, 2019), which proposes that the saggy bright band can also be attributed to other factors, such as the aggregation process, the increased precipitation intensity and the sudden decrease of RH. For unrimed snow, the response of  $\rho_{\text{hv}}$  to the melting is obviously later than X-band reflectivity, which indicates that the utilization of  $\rho_{\text{hv}}$  for detecting the ML top should be applied with caution.

The reflectivity peak is smaller for rimed snow than unrimed for a given PR, provided that the Rayleigh scattering is not violated. When  $\text{PR} > 1 \text{ mm h}^{-1}$  the reflectivity peaks of rimed and unrimed snow are closer, which can be explained by the non-Rayleigh scattering of very large aggregates at X-band as discussed by Fabry and Zawadzki (1995). Another notable finding is that the  $Z_X$  at the ML top for rimed snow is smaller than unrimed, which indicates that rimed snowflakes may have smaller sizes for a given PR. This is further confirmed in the DWR(X,Ka) profiles as shown in Fig. 5. From the aggregation region to the ML top, the DWR(X,Ka) of rimed snow is significantly smaller than unrimed snow. In particular, very weak DWR(X,Ka) for rimed snow could be identified just above the ML. This indicates that the aggregation process, the dominating factor of growing snow size close to the ML (Fabry and Zawadzki, 1995), can be heavily suppressed for rimed snow. Heymsfield et al.

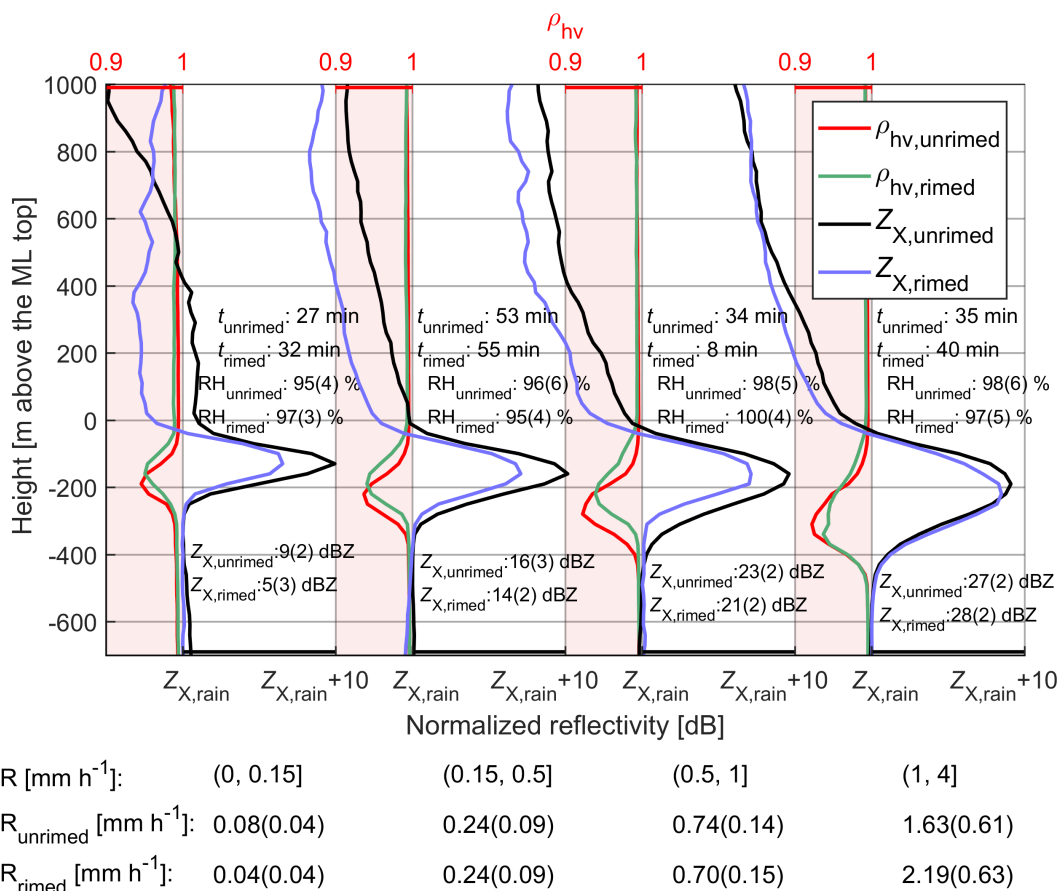


**Figure 4.** Normalized X-band radar profiles grouped by PR.  $t_{\text{unrimed}}$  and  $t_{\text{rimed}}$  indicate the total observing time in each group for unrimed and rimed cases, respectively. The median values of X-band reflectivity at the ML bottom for unrimed ( $Z_{X,\text{unrimed}}$ ) and rimed ( $Z_{X,\text{rimed}}$ ) cases are marked just below the ML bottom with the standard values in brackets. The median and standard deviations (in parentheses) of relative humidity (RH) at the ML top for unrimed ( $\text{RH}_{\text{unrimed}}$ ) and rimed ( $\text{RH}_{\text{rimed}}$ ) cases in each group are presented near the ML top. The median and standard deviations (in parentheses) of PR for unrimed ( $\text{PR}_{\text{unrimed}}$ ) and rimed ( $\text{PR}_{\text{rimed}}$ ) cases in each group are presented in the lower part.

(2015) have reported the enhanced maximum particle size below the 0°C isotherm using in-situ measurements, and attributed it to the continuing aggregation in the ML. Such continuing aggregation in conjunction with the changing scattering properties (the water coating) may be responsible for the continuing increase of DWR(X,Ka) in the ML.

#### 4.2.2 Ka-band LDR and reflectivity

- LDR usually increases in the ML, as melting is rises the dielectric constant of nonspherical ice particles. Figure 6 shows the profiles of LDR (Ka-SACR) as well as  $\rho_{\text{hv}}$  (X-SACR). Both LDR peak and  $\rho_{\text{hv}}$  dip of rimed snow are lower than unrimed

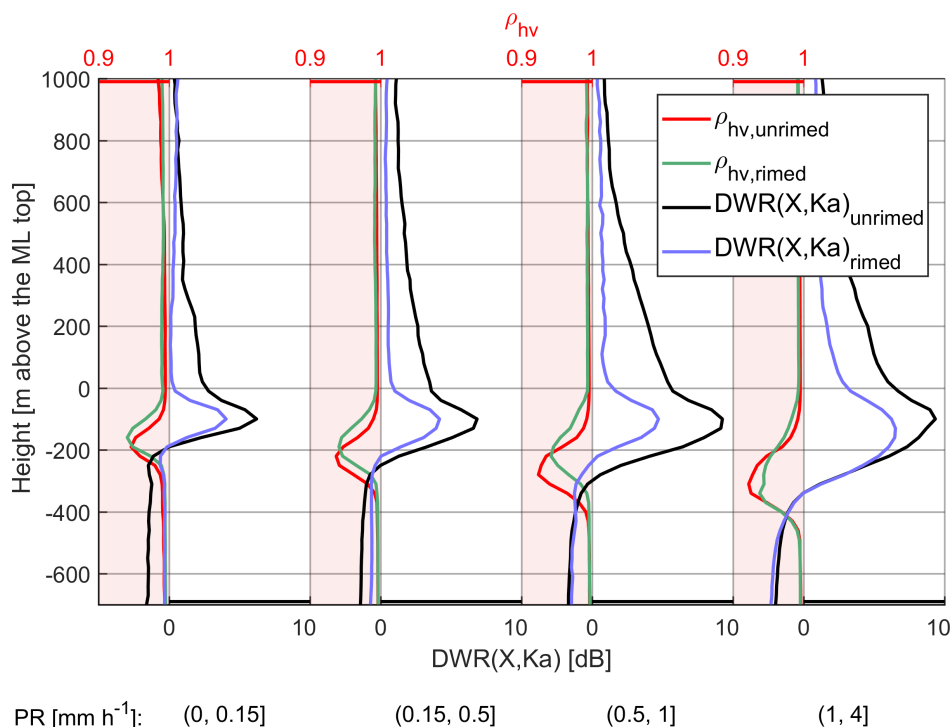


**Figure 5.** Same as Fig. 4, but for  $DWR(X,Ka)$ . Note that the radar calibration is made by matching the X- and Ka-band radar reflectivities at cloud top.

5 snow when  $PR > 1 \text{ mm h}^{-1}$ , while the reverse is observed for lighter precipitation. Despite the rather good agreement between LDR and  $\rho_{hv}$  observations, it appears that LDR systematically reveals lower ML bottom than  $\rho_{hv}$ , indicating that LDR can be suitable in discriminating rain and melting snow (Illingworth and Thompson, 2011; Dias Neto et al., 2019). The smaller LDR peak for rimed snow is correlated with the smaller X-band reflectivity enhancement as shown in Fig. 4, which is consistent with (Illingworth and Thompson, 2011; Sandford et al., 2017).

As Ka-band reflectivity can be significantly affected by the attenuation from ML, rain as well as a wet radome (Li and Moisseev, 2019). To mitigate this, the relative calibration was made at cloud top where the Rayleigh assumption can apply at Ka- and X-bands. Figure 7 shows the Ka-band reflectivity profiles. To be in line with Fig. 4,  $\rho_{hv}$  observed by X-SACR is presented instead of the LDR measured by Ka-SACR. The Ka-band reflectivity enhancement decreases as the precipitation intensifies due to the increasing non-Rayleigh scattering effect. Such effects can also explain the slightly larger enhancement of the reflectivity in the ML for rimed snow than the unrimed when  $PR > 0.5 \text{ mm h}^{-1}$ , as rimed snow is smaller for a given PR.

When  $PR \leq 0.15 \text{ mm h}^{-1}$ , a weak reflectivity dip, the dark band, appears at the top of ML for unrimed snow, which may also be observed by cm-wavelength radars Fabry and Zawadzki (1995). In literature, the dark band has different definitions. For ground-based radars, Kollias and Albrecht (2005) referred the dip of radar reflectivity below the ML top as dark band. The dark band which is present just above the ML top, as observed by the spaceborne W-band radar, can be caused by the strong

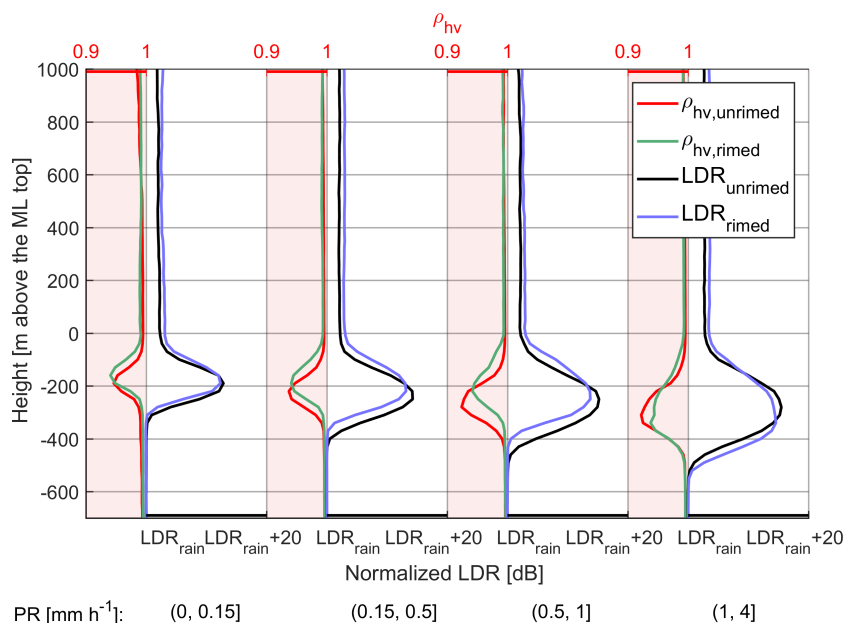


**Figure 6.** Same as Fig. 4, but for LDR observed by Ka-SACR.

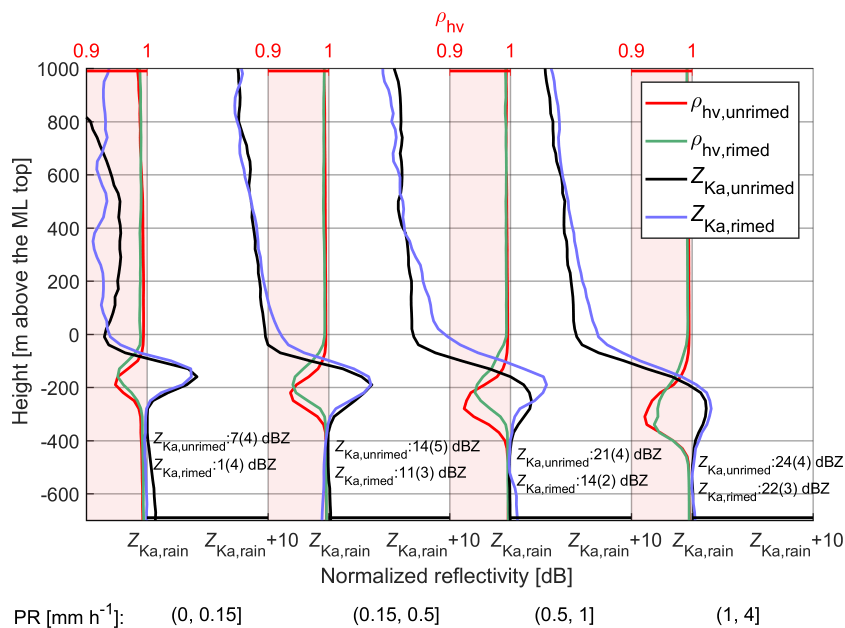


**Figure 7.** Same as Fig. 4, but for Ka-band radar. Note that the calibration is made by matching the Ka-band reflectivity with X-band at cloud top, while the attenuation in the profile is not accounted.



signal attenuation from large snow aggregates as discussed in (Sassen et al., 2007). Meanwhile, the change of PSD during the aggregation process can also contribute to this reflectivity dip, which is named dark band by Sassen et al. (2005) and dim band by Heymsfield et al. (2008). In this study, the dark band is identified as the decrease of radar reflectivity just above the ML top as shown in (Sassen et al., 2005, 2007; Heymsfield et al., 2008).

### 5 4.2.3 W-band reflectivity

W-band reflectivity can be heavily affected by a wet radome, rain, ML, supercooled liquid water and gaseous attenuation (Kneifel et al., 2015; Li and Moisseev, 2019). Such attenuation coupled with precipitation microphysical processes as well as the change of particle scattering regimes can modulate the W-band reflectivity profiles. As shown in Fig. 8, the decrease of W-band reflectivity with height is mainly caused by rain attenuation. This effect is enhanced as PR increases, which has been adopted to retrieve PR (Matrosov, 2007). From dry to melting snow, there is a jump in W-band reflectivity, and the extent of such a jump seems dependent on PR. The bright band signature is partially visible when  $PR \leq 0.15 \text{ mm h}^{-1}$  but is absent as the precipitation intensifies. This is expected, given the increased non-Rayleigh scattering at W-band for large snowflakes (Sassen et al., 2005). When  $PR \leq 0.15 \text{ mm h}^{-1}$ , the dark band is present for both unrimed and rimed snow, while the reflectivity dip near the ML top for unrimed snow is stronger than rimed. Below  $1 \text{ mm h}^{-1}$ , the dark band is present for unrimed snow, in contrast with its absence for rimed snow when  $PR > 0.15 \text{ mm h}^{-1}$ , which may indicate that the dark band is more frequently observed for the scenario of unrimed snow.

Sassen et al. (2005) have proposed that the dark band observed by W-band radars is due to the combination of Rayleigh and non-Rayleigh scattering effects modulated by the PSD. Heymsfield et al. (2008) have pinpointed that such a reflectivity dip is linked to the aggregation process, which consumes small ice while grows large snowflakes whose backscattering cross sections at W-band are much smaller than the scenario of Rayleigh scattering. This statement is evidenced in our statistical results, since the dark band feature is more significant for unrimed snow and is more distinct at W-band than at Ka-band. Furthermore, the obscured dark band for rimed snow may indicate that the aggregation of rimed snow can be weaker than unrimed snow.

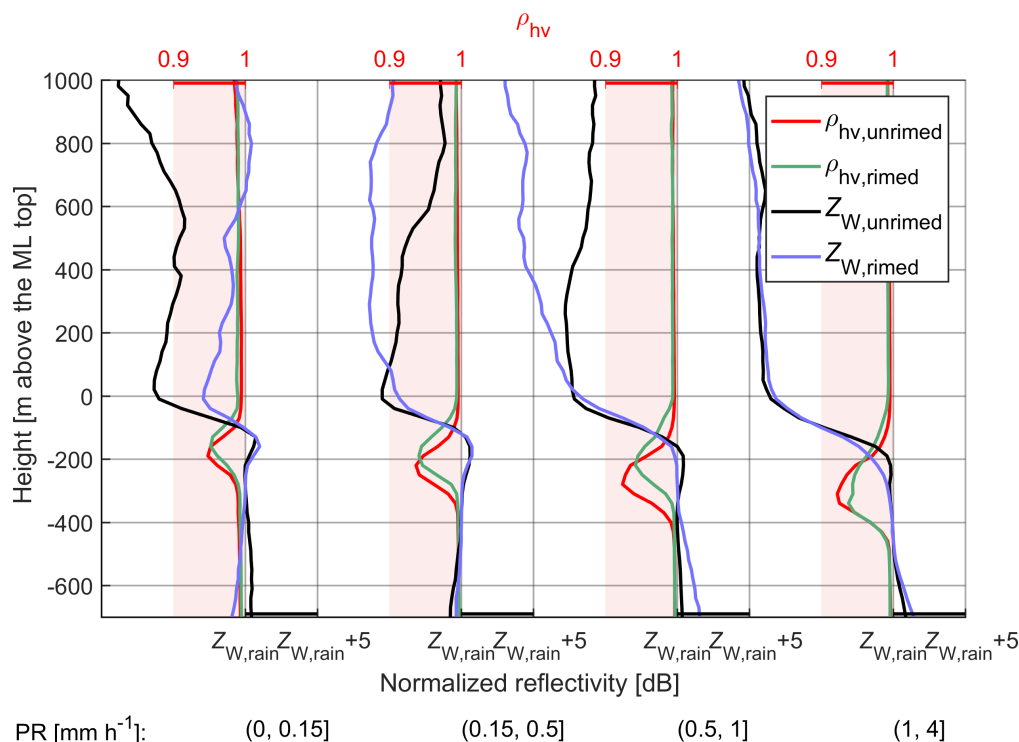


**Figure 8.** Same as Fig. 4, but for W-band. Note that  $Z_{W,rain}$  is not shown due to the unknown W-band attenuation.

### 4.3 Weather radar measurements

Recent studies have demonstrated the potential of polarimetric measurements in revealing cloud microphysics and improving precipitation forecasts (Tiira and Moisseev, 2020; Trömel et al., 2019). Given the importance of precipitation intensity to the ML, it is necessary to address how the dual-polarization observations are dependent on PR. Therefore, we have analyzed the statistical profiles of  $Z_{dr}$  and  $K_{dp}$  observed by the RHI scan of FMI C-band dual-polarization radar. The vertical axis of weather radar RHI observations was shifted to the same level as we did for vertically-pointing radars.

Significant dependence of  $Z_{dr}$  and  $K_{dp}$  on PR can be found in Fig. 9. In cases where  $PR > 0.15 \text{ mm h}^{-1}$ ,  $Z_{dr}$  decreases significantly to around 0 dB just above the ML. This is mainly due to the aggregation process, which leads to increased particle size and decreased density. In contrast,  $Z_{dr}$  does not change just above the ML when  $PR \leq 0.15 \text{ mm h}^{-1}$ , indicating that very weak aggregation happens in light precipitation. Li et al. (2018) have shown that  $Z_{dr}$  is a function of snow shape, canting angle distribution and density, and generally decreases with the increase of radar reflectivity. It would be interesting to study the riming impact on  $Z_{dr}$  profiles (Vogel and Fabry, 2018); unfortunately, we were not able to perform such a comparison due to the very limited number of RHI profiles during the studied events. It should be noted that the beam width of FMI C-band radar is  $1^\circ$ , resulting in vertical projection of around 1.1 km over the Hyytiälä station. This explains why the height of  $Z_{dr}$  starts increasing is approximately 500 m higher than the ML top determined by X-SACR.

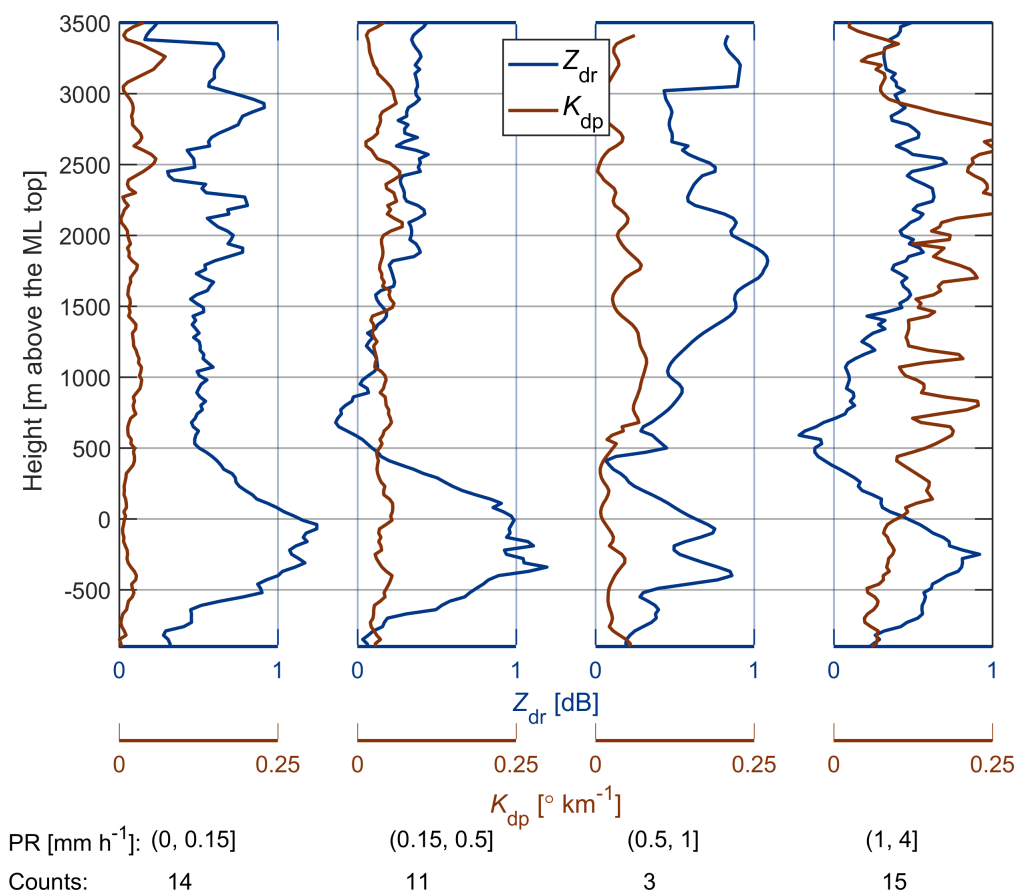


**Figure 9.** Normalized  $Z_{dr}$  and  $K_{dp}$  profiles observed by FMI C-band radar with RHI scanning. Number of RHI profiles is presented at the bottom. The ML top (as retrieved from X-SACR observations) is used as the reference height in the vertical axis.

High  $K_{dp}$  values were observed when PR exceeds  $1 \text{ mm h}^{-1}$  while no detectable  $K_{dp}$  signal can be found when  $\text{PR} \leq 1 \text{ mm h}^{-1}$ . This is in line with the previous finding that the enhanced  $K_{dp}$  is indicative of intensive precipitation (Bechini et al., 2013). When  $\text{PR} > 1 \text{ mm h}^{-1}$ , the enhanced  $K_{dp}$  starts at around 3000 m above the ML with the expected temperature of around  $-20 \text{ }^\circ\text{C}$ , which is related to the dendritic growth region (Bechini et al., 2013; Moisseev et al., 2015). Overall, these observations indicate that the dependence of ML properties on the dual-polarization signatures above, may mainly be due to correlation of these signatures with precipitation intensity.

## 5 Conclusions

In this work, the connection between the precipitation melting layer and snow microphysics was studied using vertically-pointing multi-frequency Doppler radar and C-band dual-polarization weather radar observations. Using surface-based snow-fall measurements collected over five winters at the University of Helsinki measurement station and supplemented by the single



particle scattering datasets of aggregated snowflakes and rimed ice particles, a connection between rime mass fraction and radar observations at X- and Ka-bands was established and used in classifying unrimed and rimed snow. The sanity checks show that the results of this classification are consistent with the previous study using single-frequency radar observations (Zawadzki et al., 2005). Statistics of vertically-pointing multi-frequency dual-polarization radars and RHI scans of C-band polarimetric weather radar show that

1. Precipitation intensity has a strong impact on melting layer properties. The increase in precipitation intensity can lead to the saggy bright band, i.e., the descending of reflectivity peak and  $\rho_{hv}$  dip.
2. Riming can affect melting layer properties in the following ways,
  - (a) In moderate to heavy rainfall, riming may cause additional bright band sagging. However, the opposite effect is observed in light precipitation, namely, such sagging is associated with unrimed snow.
  - (b) X-band radar reflectivity peak is smaller for rimed snow than unrimed for a given precipitation intensity, if the non-Rayleigh scattering effect is not significant.
  - (c) If the non-Rayleigh scattering effect is distinct, e.g., at Ka- or W-band, the reflectivity peak can be larger for rimed snow.
  - (d) The reflectivity dip at the melting layer top (dark band) is obscured for rimed snow, while it is pronounced for unrimed snow. This suggests that the aggregation process may be suppressed by riming.
3.  $Z_{dr}$  observed at C-band decreases during the aggregation process just above the melting layer, and can be as low as 0 dB when the precipitation rate is above  $0.15 \text{ mm h}^{-1}$ . No such changes of  $Z_{dr}$  can be identified for light precipitation.  $K_{dp}$  is not sensitive to light precipitation, but an increase is seen at around 3000 m above the ML when  $PR > 1 \text{ mm h}^{-1}$ .

A well-calibrated triple-frequency radar setup has been shown potential in studying the microphysics of snowfall. However, such measurements may not be well suited to rainfall due to the highly uncertain W-band attenuation caused by the melting layer as well as the supercooled water. The approach presented explores the possibility of adding the Doppler velocity to distinguish between unrimed and rimed conditions and is less affected by the attenuation from supercooled water. Such instrumentation as the X/Ka-SACR mounted on the same platform takes much less effort in pointing alignment. Its application may also be expanded to space-borne radars. For example, instead of launching triple-frequency radars, implementing the Doppler capability with sufficient sensitivity on either of the radars on a dual-wavelength platform may be served as an option.

A coordinated radar setup as employed during BAEC facilitates the synergy of multiple radar frequencies and polarimetric observations at various scan modes. If such coordinated measurement with high time resolution can be obtained in the future, our understanding of snow microphysical processes may be further advanced.

*Data availability.* The FMI radar data are available from the Finnish Meteorological Institute open data portal:



<http://en.ilmatiiteenlaitos.fi/open-data-sets-available>.

The ARM data used in this study are available from Atmospheric Radiation Measurement (ARM) Climate Research Facility (ARM Climate Research Facility, 2006, 2010, 2011).

PIP data are available from <https://github.com/dmoisseev/Snow-Retrievals-2014-2015>.

- 5 *Author contributions.* HL and DM designed and conceptualized the study. HL performed the investigation and did the data analysis. DM contributed with the research supervision. JT processed the FMI C-band radar raw data. AvL developed the snow retrieval algorithm based on PIP products. HL wrote the original draft. All co-authors contributed to reviewing and editing this draft.

*Competing interests.* The authors declare that they have no conflict of interest.

- 10 *Acknowledgements.* We would like to thank the personnel of Hyytiälä station for their support in field observation. Special thanks to Matti Leskinen for his help in data analysis. The research of Haoran Li, Jussi Tiira and Dmitri Moisseev were supported by the Academy of Finland Finnish Center of Excellence program (grant 307331) and ERA-PLANET, trans-national project iCUPE (grant agreement 689443), funded under the EU Horizon 2020 Framework Programme. Haoran Li was also funded by China Scholarship Council. The instrumentation used in this study was supported by NASA Global Precipitation Measurement Mission ground validation program and by the Office of Science U.S. Department of Energy ARM program.



## References

- ARM Climate Research Facility: Marine W-Band (95 GHz) ARM Cloud Radar (MWACR). 2014-01-15 to 2014-09-13, ARM Mobile Facility (TMP) U. of Helsinki Research Station (SMEAR II), Hyttiala, Finland; AMF2 (M1), Compiled by Isom B., Bharadwaj N., Lindenmaier I., Nelson D., Hardin J. and Matthews A., Atmospheric Radiation Measurement (ARM) Climate Research Facility Data Archive: Oak Ridge, Tennessee, USA, <https://doi.org/10.5439/1150242> (last access: 10 February 2018), 2006.
- ARM Climate Research Facility: Ka-Band Scanning ARM Cloud Radar (KASACRVPT). 2014-01-15 to 2014-09-13, ARM Mobile Facility (TMP) U. of Helsinki Research Station (SMEAR II), Hyttiala, Finland; AMF2 (M1), Compiled by Isom B., Bharadwaj N., Lindenmaier I., Nelson D., Hardin J. and Matthews A., Atmospheric Radiation Measurement (ARM) Climate Research Facility Data Archive: Oak Ridge, Tennessee, USA, <https://doi.org/10.5439/1046201> (last access: 10 February 2018), 2010.
- ARM Climate Research Facility: X-Band Scanning ARM Cloud Radar (XSACRVPT). 2014-01-15 to 2014-09-13, ARM Mobile Facility (TMP) U. of Helsinki Research Station (SMEAR II), Hyttiala, Finland; AMF2 (M1), compiled by: Isom B., Bharadwaj N., Lindenmaier I., Nelson D., Hardin J. and Matthews A., Atmospheric Radiation Measurement (ARM) Climate Research Facility Data Archive: Oak Ridge, Tennessee, USA, <https://doi.org/10.5439/1150303> (last access: 10 February 2018), 2011.
- Atlas, D.: Drop size and radar structure of a precipitation streamer, *Journal of Meteorology*, 14, 261–271, 1957.
- Barrett, A. I., Westbrook, C. D., Nicol, J. C., and Stein, T. H.: Rapid ice aggregation process revealed through triple-wavelength Doppler spectrum radar analysis, *Atmospheric Chemistry and Physics*, 19, 5753–5769, 2019.
- Bechini, R., Baldini, L., and Chandrasekar, V.: Polarimetric radar observations in the ice region of precipitating clouds at C-band and X-band radar frequencies, *Journal of Applied Meteorology and Climatology*, 52, 1147–1169, 2013.
- Bringi, V. N. and Chandrasekar, V.: *Polarimetric Doppler weather radar: principles and applications*, Cambridge university press, 2001.
- Carlin, J. T. and Ryzhkov, A. V.: Estimation of Melting-Layer Cooling Rate from Dual-Polarization Radar: Spectral Bin Model Simulations, *Journal of Applied Meteorology and Climatology*, 58, 1485–1508, 2019.
- Chase, R. J., Finlon, J. A., Borque, P., McFarquhar, G. M., Nesbitt, S. W., Tanelli, S., Sy, O. O., Durden, S. L., and Poellot, M. R.: Evaluation of Triple-Frequency Radar Retrieval of Snowfall Properties Using Coincident Airborne In Situ Observations During OLYMPEX, *Geophysical Research Letters*, 45, 5752–5760, 2018.
- Dias Neto, J., Kneifel, S., Ori, D., Trömel, S., Handwerker, J., Bohn, B., Hermes, N., Mühlbauer, K., Lenefer, M., and Simmer, C.: The TRIPLE-frequency and Polarimetric radar Experiment for improving process observations of winter precipitation, *Earth System Science Data*, 11, 845–863, <https://doi.org/10.5194/essd-11-845-2019>, 2019.
- Doviak, R., Bringi, V., Ryzhkov, A., Zahrai, A., and Zrnić, D.: Considerations for polarimetric upgrades to operational WSR-88D radars, *Journal of Atmospheric and Oceanic Technology*, 17, 257–278, 2000.
- Erlingis, J. M., Gourley, J. J., Kirstetter, P.-E., Anagnostou, E. N., Kalogiros, J., Anagnostou, M. N., and Petersen, W.: Evaluation of operational and experimental precipitation algorithms and microphysical insights during IPHEX, *Journal of Hydrometeorology*, 19, 113–125, 2018.
- Fabry, F. and Zawadzki, I.: Long-term radar observations of the melting layer of precipitation and their interpretation, *Journal of the Atmospheric Sciences*, 52, 838–851, 1995.
- Falconi, M. T., Lerber, A. v., Ori, D., Marzano, F. S., and Moisseev, D.: Snowfall retrieval at X, Ka and W bands: consistency of backscattering and microphysical properties using BAECC ground-based measurements, *Atmospheric Measurement Techniques*, 11, 3059–3079, 2018.



- Giangrande, S. E., Krause, J. M., and Ryzhkov, A. V.: Automatic designation of the melting layer with a polarimetric prototype of the WSR-88D radar, *Journal of Applied Meteorology and Climatology*, 47, 1354–1364, 2008.
- Giangrande, S. E., Toto, T., Bansemmer, A., Kumjian, M. R., Mishra, S., and Ryzhkov, A. V.: Insights into riming and aggregation processes as revealed by aircraft, radar, and disdrometer observations for a 27 April 2011 widespread precipitation event, *Journal of Geophysical Research: Atmospheres*, 121, 5846–5863, 2016.
- 5 Grecu, M., Tian, L., Heymsfield, G. M., Tokay, A., Olson, W. S., Heymsfield, A. J., and Bansemmer, A.: Nonparametric Methodology to Estimate Precipitating Ice from Multiple-Frequency Radar Reflectivity Observations, *Journal of Applied Meteorology and Climatology*, 57, 2605–2622, 2018.
- Haynes, J. M., L'Ecuyer, T. S., Stephens, G. L., Miller, S. D., Mitrescu, C., Wood, N. B., and Tanelli, S.: Rainfall retrieval over the ocean with spaceborne W-band radar, *Journal of Geophysical Research: Atmospheres*, 114, 2009.
- Helmus, J. J. and Collis, S. M.: The Python ARM Radar Toolkit (Py-ART), a library for working with weather radar data in the Python programming language, *Journal of Open Research Software*, 4, 2016.
- Heymsfield, A. J., Bansemmer, A., and Twohy, C. H.: Refinements to ice particle mass dimensional and terminal velocity relationships for ice clouds. Part I: Temperature dependence, *Journal of the Atmospheric Sciences*, 64, 1047–1067, 2007.
- 15 Heymsfield, A. J., Bansemmer, A., Matrosov, S., and Tian, L.: The 94-GHz radar dim band: Relevance to ice cloud properties and CloudSat, *Geophysical Research Letters*, 35, 2008.
- Heymsfield, A. J., Bansemmer, A., Poellot, M. R., and Wood, N.: Observations of ice microphysics through the melting layer, *Journal of the Atmospheric Sciences*, 72, 2902–2928, 2015.
- Heymsfield, G. M.: Doppler radar study of a warm frontal region, *Journal of the Atmospheric Sciences*, 36, 2093–2107, 1979.
- 20 Hogan, R. J., Illingworth, A. J., and Sauvageot, H.: Measuring crystal size in cirrus using 35- and 94-GHz radars, *Journal of Atmospheric and Oceanic Technology*, 17, 27–37, 2000.
- Huggel, A., Schmid, W., and Waldvogel, A.: Raindrop size distributions and the radar bright band, *Journal of Applied Meteorology*, 35, 1688–1701, 1996.
- Illingworth, A. and Thompson, R.: Radar bright band correction using the linear depolarisation ratio, in: *Proc. Eighth Int. Symp. on Weather Radar and Hydrology*, pp. 64–68, 2011.
- 25 Klaassen, W.: Radar observations and simulation of the melting layer of precipitation, *Journal of the Atmospheric Sciences*, 45, 3741–3753, 1988.
- Kneifel, S., Kulie, M., and Bennartz, R.: A triple-frequency approach to retrieve microphysical snowfall parameters, *Journal of Geophysical Research: Atmospheres*, 116, 2011.
- 30 Kneifel, S., Lerber, A., Tiira, J., Moisseev, D., Kollias, P., and Leinonen, J.: Observed relations between snowfall microphysics and triple-frequency radar measurements, *Journal of Geophysical Research: Atmospheres*, 120, 6034–6055, 2015.
- Kollias, P. and Albrecht, B.: Why the melting layer radar reflectivity is not bright at 94 GHz, *Geophysical research letters*, 32, 2005.
- Kollias, P., Jo, I., Borque, P., Tatarevic, A., Lamer, K., Bharadwaj, N., Widener, K., Johnson, K., and Clothiaux, E. E.: Scanning ARM cloud radars. Part II: Data quality control and processing, *Journal of Atmospheric and Oceanic Technology*, 31, 583–598, 2014.
- 35 Kruger, A. and Krajewski, W. F.: Two-dimensional video disdrometer: A description, *Journal of Atmospheric and Oceanic Technology*, 19, 602–617, 2002.
- Kumjian, M. R., Mishra, S., Giangrande, S. E., Toto, T., Ryzhkov, A. V., and Bansemmer, A.: Polarimetric radar and aircraft observations of saggy bright bands during MC3E, *Journal of Geophysical Research: Atmospheres*, 121, 3584–3607, 2016.



- Lamb, D. and Verlinde, J.: Physics and chemistry of clouds, Cambridge University Press, 2011.
- Leinonen, J. and Moisseev, D.: What do triple-frequency radar signatures reveal about aggregate snowflakes?, *Journal of Geophysical Research: Atmospheres*, 120, 229–239, 2015.
- Leinonen, J. and Szyrmer, W.: Radar signatures of snowflake riming: A modeling study, *Earth and Space Science*, 2, 346–358, 2015.
- 5 Leinonen, J., Kneifel, S., Moisseev, D., Tyynelä, J., Tanelli, S., and Nousiainen, T.: Evidence of nonspheroidal behavior in millimeter-wavelength radar observations of snowfall, *Journal of Geophysical Research: Atmospheres*, 117, 2012a.
- Leinonen, J., Moisseev, D., Leskinen, M., and Petersen, W. A.: A climatology of disdrometer measurements of rainfall in Finland over five years with implications for global radar observations, *Journal of Applied Meteorology and Climatology*, 51, 392–404, 2012b.
- Leinonen, J., Moisseev, D., and Nousiainen, T.: Linking snowflake microstructure to multi-frequency radar observations, *Journal of Geophysical Research: Atmospheres*, 118, 3259–3270, 2013.
- 10 Leinonen, J., Lebsock, M. D., Tanelli, S., Sy, O. O., Dolan, B., Chase, R. J., Finlon, J. A., von Lerber, A., Moisseev, D., et al.: Retrieval of snowflake microphysical properties from multifrequency radar observations, *Atmospheric Measurement Techniques*, 2018.
- Lhermitte, R. M.: Observation of rain at vertical incidence with a 94 GHz Doppler radar: An insight on Mie scattering, *Geophysical Research Letters*, 15, 1125–1128, 1988.
- 15 Li, H. and Moisseev, D.: Melting layer attenuation at Ka- and W-bands as derived from multi-frequency radar Doppler spectra observations, *Journal of Geophysical Research: Atmospheres*, 124, <https://doi.org/10.1029/2019JD030316>, 2019.
- Li, H., Moisseev, D., and von Lerber, A.: How does riming affect dual-polarization radar observations and snowflake shape?, *Journal of Geophysical Research: Atmospheres*, 123, 6070–6081, 2018.
- Liebe, H. J.: An updated model for millimeter wave propagation in moist air, *Radio Science*, 20, 1069–1089, 1985.
- 20 Locatelli, J. D. and Hobbs, P. V.: Fall speeds and masses of solid precipitation particles, *Journal of Geophysical Research*, 79, 2185–2197, 1974.
- Mason, S., Chiu, C., Hogan, R., Moisseev, D., and Kneifel, S.: Retrievals of Riming and Snow Density From Vertically Pointing Doppler Radars, *Journal of Geophysical Research: Atmospheres*, 123, 13–807, 2018.
- Mason, S. L., Hogan, R. J., Westbrook, C. D., Kneifel, S., Moisseev, D., and Terzi, L. v.: The importance of particle size distribution and internal structure for triple-frequency radar retrievals of the morphology of snow, *Atmospheric Measurement Techniques*, 12, 4993–5018, 2019.
- 25 Matrosov, S. Y.: A dual-wavelength radar method to measure snowfall rate, *Journal of Applied Meteorology*, 37, 1510–1521, 1998.
- Matrosov, S. Y.: Potential for attenuation-based estimations of rainfall rate from CloudSat, *Geophysical research letters*, 34, 2007.
- Matrosov, S. Y.: Assessment of radar signal attenuation caused by the melting hydrometeor layer, *IEEE Transactions on Geoscience and Remote Sensing*, 46, 1039–1047, 2008.
- 30 Moisseev, D., von Lerber, A., and Tiira, J.: Quantifying the effect of riming on snowfall using ground-based observations, *Journal of Geophysical Research: Atmospheres*, 122, 4019–4037, 2017.
- Moisseev, D., Lautaportti, S., Alku, L., Tabakova, K., O’Connor, E. J., Leskinen, M., and Kulmala, M.: Inadvertent Localized Intensification of Precipitation by Aircraft, *Journal of Geophysical Research: Atmospheres*, 124, 2094–2104, <https://doi.org/10.1029/2018JD029449>, <https://agupubs.onlinelibrary.wiley.com/doi/abs/10.1029/2018JD029449>, 2019.
- 35 Moisseev, D. N., Lautaportti, S., Tyynelä, J., and Lim, S.: Dual-polarization radar signatures in snowstorms: Role of snowflake aggregation, *Journal of Geophysical Research: Atmospheres*, 120, 12 644–12 655, 2015.



- Morrison, H. and Milbrandt, J. A.: Parameterization of cloud microphysics based on the prediction of bulk ice particle properties. Part I: Scheme description and idealized tests, *Journal of the Atmospheric Sciences*, 72, 287–311, 2015.
- Newman, A. J., Kucera, P. A., and Bliven, L. F.: Presenting the snowflake video imager (SVI), *Journal of Atmospheric and Oceanic technology*, 26, 167–179, 2009.
- 5 Oue, M., Kollias, P., Ryzhkov, A., and Luke, E. P.: Toward exploring the synergy between cloud radar polarimetry and Doppler spectral analysis in deep cold precipitating systems in the Arctic, *Journal of Geophysical Research: Atmospheres*, 123, 2797–2815, 2018.
- Petäjä, T., O’Connor, E. J., Moisseev, D., Sinclair, V. A., Manninen, A. J., Väänänen, R., von Lerber, A., Thornton, J. A., Nicoll, K., Petersen, W., et al.: BAECC: A field campaign to elucidate the impact of biogenic aerosols on clouds and climate, *Bulletin of the American Meteorological Society*, 97, 1909–1928, 2016.
- 10 Ryde, J.: The attenuation and radar echoes produced at centimeter wavelengths by various meteorological phenomena., *Meteorological Factors in Radio Wave Propagation*, London, pp. 169–189, 1946.
- Ryzhkov, A., Zhang, P., Reeves, H., Kumjian, M., Tschallener, T., Trömel, S., and Simmer, C.: Quasi-vertical profiles—A new way to look at polarimetric radar data, *Journal of Atmospheric and Oceanic Technology*, 33, 551–562, 2016.
- Sandford, C., Illingworth, A., and Thompson, R.: The potential use of the linear depolarization ratio to distinguish between convective and stratiform rainfall to improve radar rain-rate estimates, *Journal of Applied Meteorology and Climatology*, 56, 2927–2940, 2017.
- 15 Sarma, A. C., Deshamukhya, A., Narayana Rao, T., and Sharma, S.: A study of raindrop size distribution during stratiform rain and development of its parameterization scheme in the framework of multi-parameter observations, *Meteorological Applications*, 23, 254–268, 2016.
- Sassen, K., Campbell, J. R., Zhu, J., Kollias, P., Shupe, M., and Williams, C.: Lidar and triple-wavelength Doppler radar measurements of the melting layer: A revised model for dark-and brightband phenomena, *Journal of Applied Meteorology*, 44, 301–312, 2005.
- Sassen, K., Matrosov, S., and Campbell, J.: CloudSat spaceborne 94 GHz radar bright bands in the melting layer: An attenuation-driven upside-down lidar analog, *Geophysical Research Letters*, 34, 2007.
- Sekelsky, S. M.: Near-field reflectivity and antenna boresight gain corrections for millimeter-wave atmospheric radars, *Journal of Atmospheric and Oceanic Technology*, 19, 468–477, 2002.
- 25 Stewart, R. E., Marwitz, J. D., Pace, J. C., and Carbone, R. E.: Characteristics through the melting layer of stratiform clouds, *Journal of the Atmospheric Sciences*, 41, 3227–3237, 1984.
- Szeto, K. K., Lin, C. A., and Stewart, R. E.: Mesoscale circulations forced by melting snow. Part I: Basic simulations and dynamics, *Journal of the Atmospheric Sciences*, 45, 1629–1641, 1988.
- Szyrmer, W. and Zawadzki, I.: Modeling of the melting layer. Part I: Dynamics and microphysics, *Journal of the Atmospheric Sciences*, 56, 3573–3592, 1999.
- 30 Tiira, J. and Moisseev, D. N.: Unsupervised classification of vertical profiles of dual polarization radar variables, *Atmospheric Measurement Techniques*, 13, 1227–1241, 2020.
- Tiira, J., Moisseev, D. N., von Lerber, A., Ori, D., Tokay, A., Bliven, L. F., and Petersen, W.: Ensemble mean density and its connection to other microphysical properties of falling snow as observed in Southern Finland, *Atmospheric Measurement Techniques*, 9, 2016.
- 35 Trömel, S., Ryzhkov, A. V., Zhang, P., and Simmer, C.: Investigations of backscatter differential phase in the melting layer, *Journal of Applied Meteorology and Climatology*, 53, 2344–2359, 2014.



- Trömel, S., Ryzhkov, A. V., Hickman, B., Mühlbauer, K., and Simmer, C.: Polarimetric radar variables in the layers of melting and dendritic growth at X band—implications for a nowcasting strategy in stratiform rain, *Journal of Applied Meteorology and Climatology*, **58**, 2497–2522, 2019.
- 5 Tyynelä, J. and Chandrasekar, V.: Characterizing falling snow using multifrequency dual-polarization measurements, *Journal of Geophysical Research: Atmospheres*, **119**, 8268–8283, 2014.
- Tyynelä, J. and von Lerber, A.: Validation of microphysical snow models using in-situ, multi-frequency and dual-polarization radar measurements in Finland, **124**, 13 273–13 290, <https://doi.org/10.1029/2019JD030721>, <https://agupubs.onlinelibrary.wiley.com/doi/abs/10.1029/2019JD030721>, 2019.
- 10 Vogel, J. M. and Fabry, F.: Contrasting Polarimetric Observations of Stratiform Riming and Nonriming Events, *Journal of Applied Meteorology and Climatology*, **57**, 457–476, 2018.
- von Lerber, A., Moisseev, D., Leinonen, J., Koistinen, J., and Hallikainen, M. T.: Modeling radar attenuation by a low melting layer with optimized model parameters at C-band, *IEEE Transactions on Geoscience and Remote Sensing*, **53**, 724–737, 2014.
- von Lerber, A., Moisseev, D., Bliven, L. F., Petersen, W., Harri, A.-M., and Chandrasekar, V.: Microphysical properties of snow and their link to Z e–S relations during BAECC 2014, *Journal of Applied Meteorology and Climatology*, **56**, 1561–1582, 2017.
- 15 Willis, P. T. and Heymsfield, A. J.: Structure of the melting layer in mesoscale convective system stratiform precipitation, *Journal of the Atmospheric Sciences*, **46**, 2008–2025, 1989.
- Wolfensberger, D., Scipion, D., and Berne, A.: Detection and characterization of the melting layer based on polarimetric radar scans, *Quarterly Journal of the Royal Meteorological Society*, **142**, 108–124, 2016.
- 20 Xie, X., Evaristo, R., Simmer, C., Handwerker, J., and Trömel, S.: Precipitation and microphysical processes observed by three polarimetric X-band radars and ground-based instrumentation during HOPE, *Atmospheric Chemistry and Physics*, **16**, 7105–7116, 2016.
- Zawadzki, I., Szyrmer, W., Bell, C., and Fabry, F.: Modeling of the melting layer. Part III: The density effect, *Journal of the Atmospheric Sciences*, **62**, 3705–3723, 2005.